Energy & Environmental Science

ROYAL SOCIETY OF CHEMISTRY

PAPER

View Article Online
View Journal | View Issue

Cite this: *Energy Environ. Sci.*, 2024, **17**, 1904

Ultrahigh *zT* from strong electron–phonon interactions and a low-dimensional Fermi surface†

V. K. Ranganayakulu,‡[abc] Te-Hsien Wang, ‡[d] Cheng-Lung Chen, *[ef] Angus Huang,[ghi] Ma-Hsuan Ma,[j] Chun-Min Wu,[k] Wei-Han Tsai,[ac] Tsu-Lien Hung,[a] Min-Nan Ou, [a] Horng-Tay Jeng, *[agi] Chih-Hao Lee, [b] Kuei-Hsien Chen, [l] Wen-Hsien Li,[j] Madison K. Brod,[m] G. Jeffrey Snyder [m] and Yang-Yuan Chen *[an]

Received 5th December 2023,
Accepted 25th January 2024

DOI: 10.1039/d3ee04187e

rsc.li/ees

The outstanding thermoelectric performance of GeTe has attracted significant attention in the research community in recent years. However, many of the underlying physical mechanisms that contribute to GeTe's exceptionally high figure of merit (*zT*) remain not fully understood. In this study, an Sb–Bi codoped GeTe single crystal $(Ge_{0.86}Sb_{0.08}Bi_{0.06})Te$ with an ultrahigh *zT* of 2.7 at 700 K and a record high device *zT* of 1.41 in the temperature range of 300–773 K was synthesized and investigated. The ultrahigh *zT* is attributed to the extremely low lattice thermal conductivity induced by strong electron–phonon (EP) interactions as revealed by the experimentally observed Kohn anomaly, through inelastic neutron scattering (INS) measurements. First-principles calculations further demonstrate that the remarkable EP interaction arises from the Fermi surface nesting featured in a one-dimensional (double-walled) topology. Our finding unravels the ultrahigh-*zT* mechanism in GeTe-based materials, serving as an inspiring guide toward high thermoelectric performance.

Broader context

In nature, the most efficient thermoelectric materials, exhibiting high thermoelectric figures of merit (*zT*), typically involve polycrystalline structures achieved by minimizing thermal conductivity through nanostructuring to enhance interface scattering. However, a notable exception arises with single-crystal hole-doped SnSe, where $zT > 2$ has been achieved. Nonetheless, there are underlying aspects related to the fundamental role of phonons that remain unaddressed and require resolution. In this study, we prepared single crystals of pristine GeTe and Sb–Bi co-doped GeTe to elucidate the unique nesting features of the Fermi surface. This exploration provides insights into electron–phonon scattering and modifies the phonon density of states in Sb–Bi co-doped systems, shedding light on how to induce exceptionally strong electron–phonon interactions, thereby impeding phonon propagation. Our findings pave the way for a novel approach to phonon engineering in single-crystal thermoelectric materials, extending beyond conventional nanostructuring techniques.

[a] *Institute of Physics, Academia Sinica, Taipei 11529, Taiwan. E-mail: jeng@phys.nthu.edu.tw, cheny2@phys.sinica.edu.tw*
[b] *Department of Engineering and System Science, National Tsing Hua University, Hsinchu 30013, Taiwan*
[c] *Taiwan International Graduate Program, Taipei 11529, Taiwan*
[d] *Department of Physics, National Chung Hsing University, Taichung City 40227, Taiwan*
[e] *Graduate School of Materials Science, National Yunlin University of Science and Technology, Yunlin 64002, Taiwan. E-mail: clchen0417@gmail.com*
[f] *Bachelor Program in Semiconductor Materials and Fabrication, Ming Chi University of Technology, New Taipei City 243303, Taiwan*
[g] *Department of Physics, National Tsing Hua University, Hsinchu 30013, Taiwan*
[h] *Center for Theory and Computation, National Tsing Hua University, Hsinchu 30013, Taiwan*
[i] *Physics Division, National Center for Theoretical Sciences, Taipei 10617, Taiwan*
[j] *Department of Physics, National Central University, Jhongli 32001, Taiwan*
[k] *National Synchrotron Radiation Research Center, Hsinchu Science Park, Hsinchu 30076, Taiwan*
[l] *Institute of Atomic and Molecular Sciences, Academia Sinica, Taipei 10617, Taiwan*
[m] *Department of Materials Science and Engineering, Northwestern University, Evanston, Illinois 60208, USA*
[n] *Graduate Institute of Applied Physics, National Chengchi University, Taipei 11605, Taiwan*

† Electronic supplementary information (ESI) available. See DOI: https://doi.org/10.1039/d3ee04187e

‡ V. K. R. and T. H. W. contributed equally to this work.

Introduction

Facing global climate change and the urgent need for carbon reduction, the development of renewable energy has become an even more pressing mission than ever before. Thermoelectric (TE) materials, which enable the direct and reversible conversion between heat and electricity, hold high potential to become one of the promising technologies for solving the energy crisis.[1–3] The TE performance of materials is generally evaluated by the dimensionless figure-of-merit $zT = \frac{S^2\sigma T}{\kappa}$, where S, T, σ, and κ represent the Seebeck coefficient, absolute temperature, and electrical and thermal conductivity, respectively. The thermal conductivity κ is the sum of the electronic (κ_e) and lattice (κ_{lat}) contributions, given by $\kappa = \kappa_e + \kappa_{lat}$. Most of the thermoelectric materials, such as Bi_2Te_3, Zn_4Sb_3, $CoSb_3$, Mg_3Sb_2, and SiGe, have thermoelectric zT values that are less than 2.0.[4,5] However, for a few examples like PbTe and Cu_2Se, their highest zT values can exceed 2.0.[6–8] Moreover, in the case of alloy materials like $AgSbTe_2$, SnSe, and GeTe, they have achieved remarkably high zT values surpassing 2.5.[9–13] It would be worth noting that extremely high values of ionic figure of merit (>8.5) have been reported in ionic thermoelectric materials, in which charge transport can occur through ions or mixed carriers.[14–18] However, ionic transport and electronic transport lead to very different properties and applications.[19] Thus, these ionic thermoelectric materials may fall beyond the scope of the following discussion.

It has been observed that materials with higher valley degeneracy (N_V) tend to exhibit higher quality factors and consequently higher zT values.[20,21] This is due to the presence of a larger number of available electron states, which can enhance the thermoelectric performance. The concept of valley degeneracy and its impact on zT was initially introduced by Hicks and Dresselhaus, who demonstrated that reducing the dimensionality of materials can qualitatively alter the electronic density of states (DOS) around the band edge (Fig. S1, ESI†) and lead to an increase in the Seebeck coefficient.[22,23] This low-dimensional strategy has inspired extensive research on thermoelectric materials with nanostructures and the pursuit of band convergence.[24–26] Although the DOS can be qualitatively altered by physically reducing the dimensionality in a material, the effective band degeneracy, on the contrary, would be reduced due to subband splitting explaining the lack of an improved peak power factor found experimentally in nanoscale systems.[27,28] Recent theoretical works have pointed to the discovery of materials with features of low-dimensional electronic structures in bulk materials.[29–31] For two- (one-) dimensional electronic structures, the electronic band is highly k dependent along only two (one) axes (axis). This, as illustrated in Fig. 1(a), leads to the DOS similar to that in thin films (nanowires) but without subband splitting leading potentially to extremely high effective band degeneracy.

Recent studies further show that the nesting feature of parallel sheets of the Fermi surface will trigger unusually strong EP interactions that suppress phonon heat transport. EP scattering which is generally observed at low temperatures has recently been found to play an important role in phonon heat transport of certain doped semiconductors, especially above room temperature.[32–34] In the metallic niobium carbide, a two-orders-of-magnitude reduction in lattice thermal conductivity is predicted because of the EP interaction.[34] In the

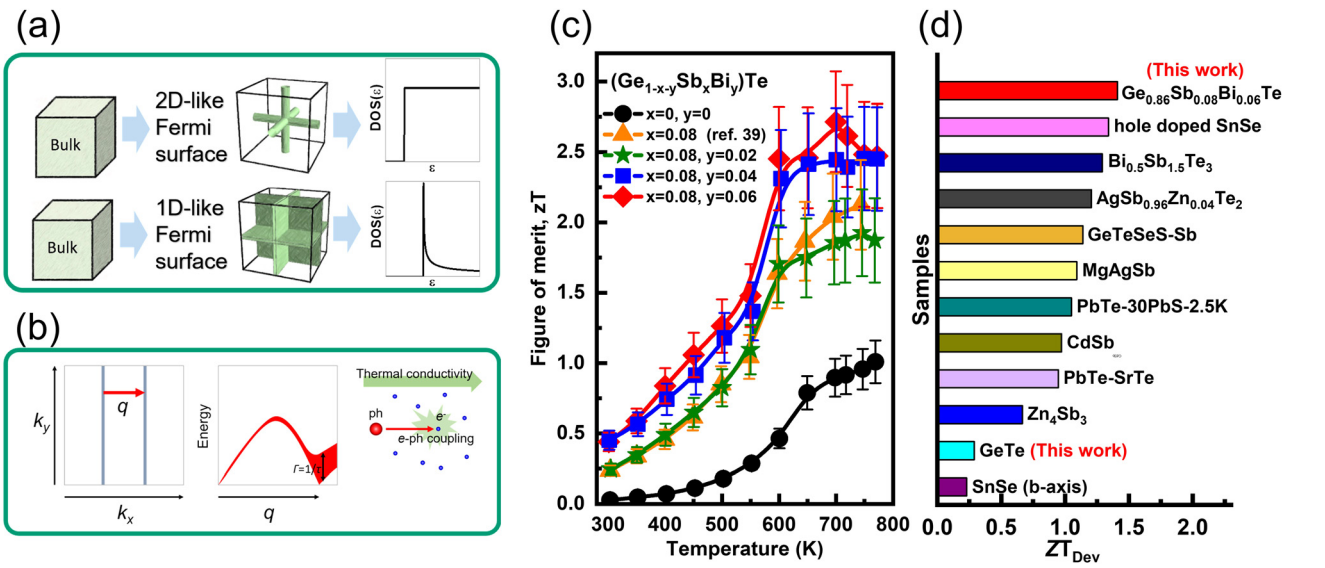

Fig. 1 Thermoelectric figure of merit of GeTe and the schematic illustration of the electron–phonon scattering mechanisms therein. (a) Schematic diagram illustrating the features of the Fermi surface and DOS exhibited by a bulk material with a 2D- or 1D-like electronic structure. (b) Fermi nesting vector $\boldsymbol{q}$ connecting two parallel 1D-like Fermi surfaces (left panel) would lead to Kohn anomaly with phonon softening and widened phonon linewidth (middle panel), indicating strong electron–phonon interactions with enhanced phonon scattering-derived low lattice thermal conductivity (right panel). (c) Temperature dependence of the zT values of $(Ge_{1-x-y}Sb_xBi_y)Te$ crystals. (d) The device ZT_{Dev} for the 300–773 K temperature range in $Ge_{0.86}Sb_{0.08}Bi_{0.06}Te$ and other known thermoelectric materials reported in previous literature.

semi-metallic 1T-TaS_2 and the semiconducting $Pb_7Bi_4Se_{13}$, EP scattering stronger than phonon–phonon scattering is suggested above the Debye temperature by the measured nearly-temperature-independent lattice thermal conductivity, which is as low as $\sim$1 Wm^{-1} K^{-1}.[35,36] The presence of a 1D-like electronic structure in a bulk material would result in Fermi surface nesting leading to strong electron–phonon (EP) coupling, which would be manifested by Kohn anomaly,[37] and lead to a significant reduction in lattice thermal conductivity as schematically illustrated in Fig. 1(b).

In this work, we combined experiments and theory to demonstrate the emergence of a strong EP interaction in a precisely tuned GeTe crystal through Sb–Bi codoping. The unique low-dimensional Fermi surface feature and enhanced EP scattering significantly improve the thermoelectric performance of GeTe. As a result, one of the highest zT values of 2.7 at 700 K in GeTe-based materials is achieved (Fig. 1(c)).[38,39] Moreover, a broad temperature plateau with a high $zT >$ 2.5 is realized in Sb–Bi codoped $(Ge_{1-x-y}Sb_xBi_y)Te$ single crystals (referred to as GSBT) from 600 to 770 K. The device ZT, estimated to be 1.41 using Snyder's model,[40] from 300 to 773 K, is the highest ever reported for most state-of-the-art p-type thermoelectric materials (Fig. 1(d)).[41–49] The thermal-to-electric conversion efficiency of $Ge_{0.86}Sb_{0.08}Bi_{0.06}Te$ is approximately 17.4%, which is higher than that of other high-zT thermoelectric materials and enhances its commercial competitiveness.[10] Our finding highlights the important role of nested planar Fermi surfaces in suppressing the lattice thermal conductivity and modulating the electrical properties for high zT thermoelectric materials.

Results and discussion

In this work, we utilized the Bridgman method to grow a series of GSBT single crystals, allowing us to systematically explore the influence of dopants on thermoelectric properties. The thermoelectric behavior of Bi-doped GeTe closely resembles that of Sb-doped GeTe, although 8% Sb doping ($Ge_{1-x}Sb_xTe$, x = 0.08) exhibits slightly better thermoelectric performance.[39,50] We observed that if GeTe is doped with more than 10% of Sb or Bi individually, and then precipitates tend to form. However, by codoping Sb and Bi in GeTe crystals, we will be able to achieve the total solubility of up to 14% (x = 0.08, y = 0.06), which is not feasible by single doping of Bi or Sb. We expect that the enhanced solubility in the co-doped system is closely linked to the concept that the solubility in alloys can be significantly elevated through the augmentation of elemental species, driven by entropy-driven structural stabilization. This phenomenon has been consolidated and referred to as high-entropy materials.[38] At room temperature, all samples exhibit the rhombohedral phase ($R3m$) with nanoscale herringbone-like domains (structural characterization and microstructures are summarized in Fig. S4–S8, ESI†). Sb and Sb–Bi codoping effectively reduce the rhombohedral-to-cubic phase transition temperatures (T_c) from 675 K to 600 K (Fig. S6 and S7, ESI†). The electrical conductivity (σ) and Seebeck coefficient (S) of all samples, as shown in Fig. 2, exhibit the expected characteristic of a degenerate p-type semiconductor, with holes as dominant charge carriers. Sb single doping or Sb–Bi codoping significantly lowers σ and enhances S. The temperature dependence of the power factor of GSBT crystals is presented in Fig. 2(c). Although the maximum power factor for the $(Ge_{0.86}Sb_{0.08}Bi_{0.06})Te$ crystal is approximately 38 μW cm^{-1} K^{-2} at 770 K, which is lower than 48 μW cm^{-1} K^{-2} for pristine GeTe and $\sim$56 μW cm^{-1} K^{-2} for the 8% Sb-doped crystal,[39] the zT of the $(Ge_{0.86}Sb_{0.08}Bi_{0.06})Te$ crystal is still significantly enhanced owing to its ultralow thermal conductivity, as shown in Fig. 2(d).

Ultralow lattice thermal conductivity

The pristine GeTe exhibits a relatively high thermal conductivity κ of $\sim$9 W m^{-1} K^{-1} at 300 K, which decreases rapidly with an increase in temperature (Fig. 2(d)) due to the significant reduction in both the electronic and lattice contributions. The decline in electronic contribution κ_e with temperature (Fig. S16, ESI†) is attributed to intensified EP scattering at high temperatures, resulting in reduced carrier mobility. The lattice thermal conductivity of pristine GeTe, as illustrated in Fig. 3(a), also decreases with temperature except around 675 K, corresponding to the rhombohedral-cubic phase transition. This behavior is typical of phonon–phonon scattering, as the number of phonons increases with an increase in temperature, indicating that phonon–phonon scattering serves as the primary intrinsic limitation to lattice thermal conductivity.

While for Sb–Bi codoped specimens, both electronic and lattice thermal conductivities experience significant reduction. The electronic thermal conductivity κ_e, as shown in Fig. S16 (ESI†), undergoes a drastic reduction to approximately 0.55 W m^{-1} K^{-1}, primarily due to the decreased hole concentration. The lattice thermal conductivity, as depicted in Fig. 3(a), decreases to values generally smaller than the amorphous limit of 0.45 W m^{-1} K^{-1} observed in GeTe.[51,52] More intriguingly, near-temperature independence character indicates that dominant scattering mechanisms are characterized by a nearly temperature-independent mean free path. Lattice imperfections present a possible scattering mechanism, as they are generally insensitive to temperature, except during phase transition or near the melting point. Another potential scattering mechanism is the EP interaction, as the number of conduction carriers in degenerate semiconductors is only weakly dependent on temperature.

As shown in Fig. 3(b), the materials show quite complex herringbone nanostructures, which could significantly reduce lattice thermal conductivity. Nevertheless, our specimens, as shown in the high-resolution transmission electron microscopy (HRTEM) images (Fig. 3(c)) and the XRD patterns (Fig. S4c and S6c, ESI†), are single crystals, which are quite far from amorphous, and thus lattice imperfection alone is unlikely to cause lattice thermal conductivity lower than the amorphous limit. From the HRTEM images, we found that the herringbone nanostructure is mainly composed of layer defects of Ge vacancies or stacking faults, in which the distances between neighboring defect layers are generally larger than 6 nm.

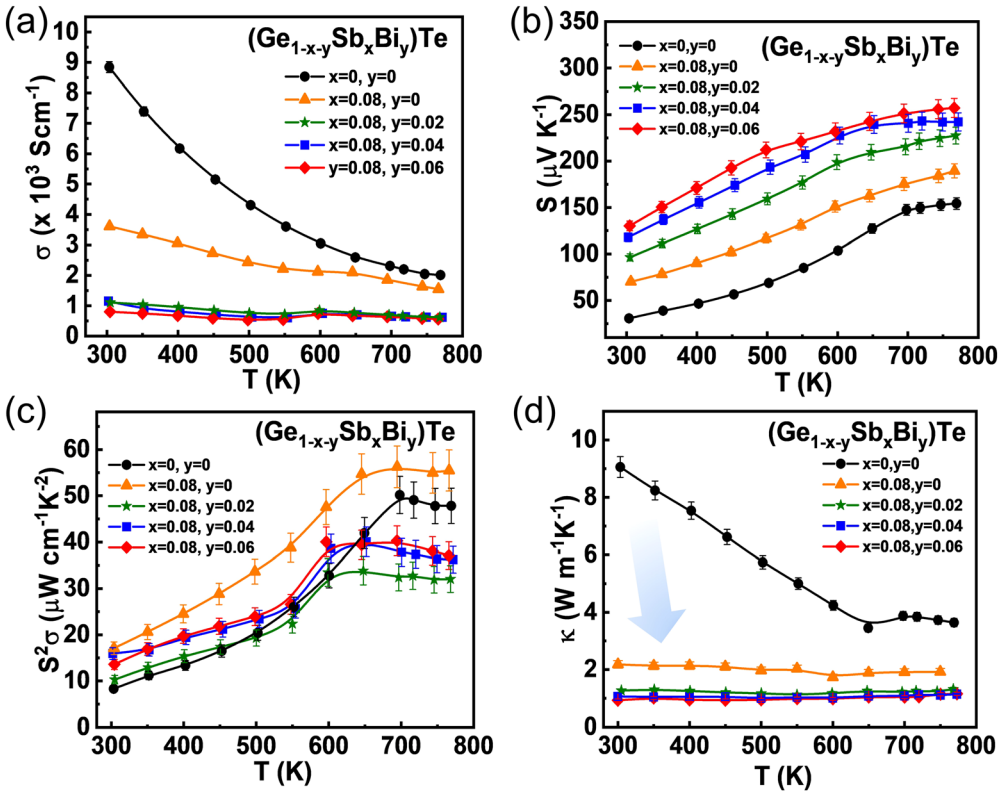

Fig. 2 Temperature dependence of the thermoelectric properties of pristine, Sb single doped, and Sb–Bi codoped GeTe crystals. (a) Electrical conductivity. (b) Seebeck coefficient. (c) Power factor. (d) Total thermal conductivity.

If these layer defects are the main causes of limiting the lattice thermal conductivity, the average phonon mean free path should be larger than, at least comparable with, 6 nm because these defect layers should be not able to completely block the phonons but deflect them. However, as discussed in the ESI† (statistically representative value of the phonon mean free path), the statistically representative value of the phonon mean free path is about 1.0 nm, which is generally more than 6 times smaller than the distance between the observed defect layers. Thus, the defect layer alone should not be able to explain the observed extremely low and nearly temperature-independent lattice thermal conductivity in Sb–Bi codoped GeTe, and there should be other significant phonon scattering mechanisms in this material system. It is worth mentioning that the suppression of κ_{lat} in the Sb–Bi codoped GeTe single crystal is so remarkable that even comparable to high-entropy GeTe-based materials that also have a high zT value but need to be doped with multiple elements (Fig. 3(d)).[38]

The ultralow thermal conductivity observed in Sb–Bi codoped GeTe with a high zT value has been confirmed through measurements. However, the fundamental mechanism underlying the strong phonon scattering in this single crystal material remains unknown. By conducting INS measurements and employing first-principles simulations, we have discovered a distinctive EP interaction that contributes to the unusually low thermal conductivity of GSBT. To gain a quantitative understanding of the behavior of lattice thermal conductivity (κ_{lat}), we initially modeled the temperature-dependent κ_{lat} of pristine GeTe, single-doped GeTe, and Sb–Bi codoped GeTe crystals using the Debye–Callaway model.[53] The theoretical fitting of κ_{lat} for pristine and single-doped GeTe agreed well with the experimental data, without considering the EP contribution. However, in the case of Sb–Bi codoped GeTe, the EP contribution needed to be incorporated into the model to achieve a good match between theory and experiment. Fig. 3(e) illustrates the comparison, where the green dotted line represents the theoretical fitting without considering EP, while the pink dotted line incorporates the contribution of EP. Further information on the detailed fitting equations and parameters for calculating phonon propagation can be found in the ESI† and Tables S2, S3. The analysis suggests that, in addition to the stacking fault (SF) defects, EP scattering plays a crucial role in scattering phonons across a wide frequency range, resulting in the observed extremely low lattice thermal conductivity. To provide further evidence and insights, we verify this significant physical phenomenon through neutron experimental measurements and theoretical calculations.

Strong electron–phonon interactions revealed by inelastic neutron scattering measurements

The strong EP interaction in the rhombohedral $R3m$ phase of the $(Ge_{0.86}Sb_{0.08}Bi_{0.06})Te$ material is experimentally confirmed through INS measurements. The peak widths of two phonon excitations, one at E = 6.72 meV (with a full width at half

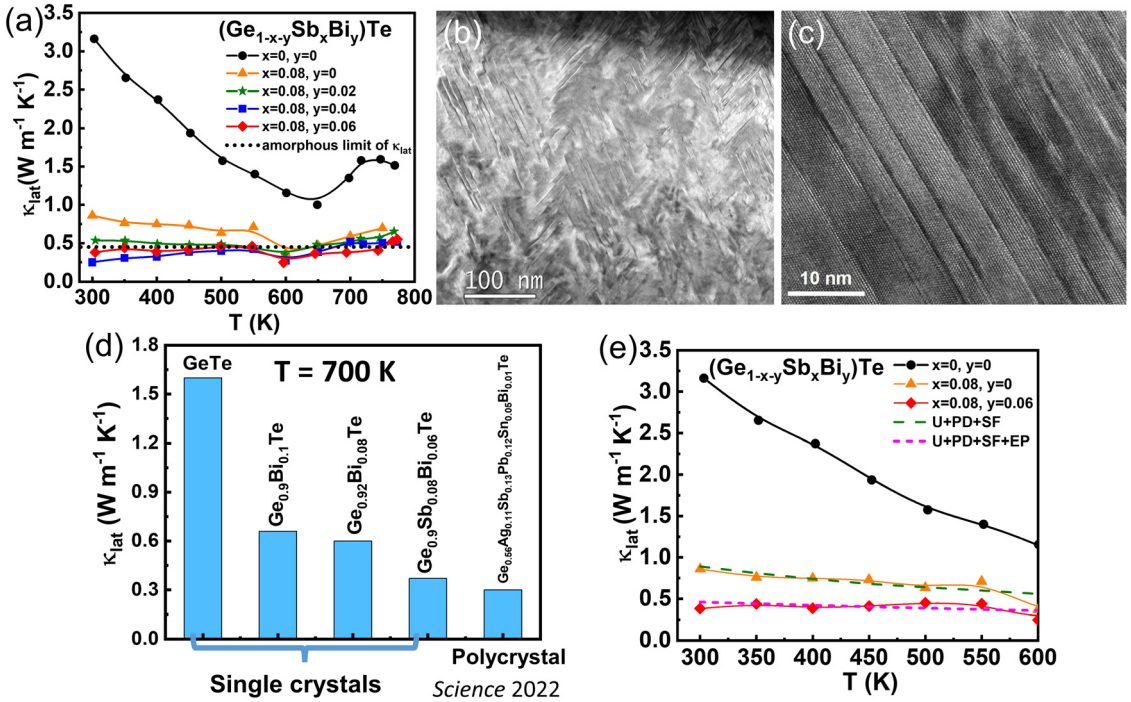

Fig. 3 Lattice thermal conductivity and microstructures. (a) Lattice thermal conductivity. (b) Low magnification TEM image. (c) A number of periodic staking faults (boundaries of two-dimensional Bi–Te/Sb–Te layers) represented by dark lines, one of which is marked with a white arrow. (d) The κ_{lat} at 700 K for single crystals and polycrystal GeTe alloys. (e) Experimental and theoretical κ_{lat} values for GeTe, $Ge_{0.92}Sb_{0.08}Te$, and $(Ge_{0.86}Sb_{0.08}Bi_{0.06})Te$ represented by dots and lines, respectively. Solid lines are B-spline curves connecting the experimental data points. The Green dashed line for single doped GeTe is derived from the Debye–Callaway model without considering EP. The pink dashed line for codoped GeTe is derived from the Debye–Callaway model with EP included.

maximum W = 2.64 meV) and the other at 12.21 meV (W = 1.67 meV), observed at H = 0.3, are significantly broader than the instrumental resolution (W = 0.052 meV). This broadening indicates a short lifetime for both the transverse acoustic (TA) phonon at 6.72 meV and the longitudinal acoustic (LA) phonon at 12.21 meV propagating along the [110] direction (filled triangles in Fig. 4(a)). Furthermore, the TA and LA phonons exhibit a reduction in energy to 4.94 and 11.34 meV, respectively, when measured at H = 0.5 (open circles in Fig. 4(a)), indicating a downturn in phonon energy as the wave vector approaches the zone boundary. The phonon dispersion along the crystallographic [110] in the rhombohedral $R3m$ phase (Fig. 4(b)) reveals two acoustic phonon dispersions: the lower-energy TA mode and the higher-energy LA mode. The colors in the map represent the scattering intensity, with the scale bar provided on the side. Each open circle with an error bar represents the excitation peak position in the excitation spectra. Both TA and LA modes exhibit energy downturns when the phonon wave vector reaches approximately 70% of the zone boundary.

The softening of phonon energy in the harmonic dispersion indicates the presence of an interaction that scatters and absorbs phonons. In contrast, the phonon dispersion of pristine GeTe at 300 K does not exhibit significant bending in the TA and LA modes[54] (Fig. S19, ESI†). To model the dispersions, it appears that the interaction can be expressed by q^2-dependency. In addition, an intrinsic component that specifies the appearance of lattice anharmonicity is also needed in describing the dispersions. Allowing a q-term plus a q^3-term for the dispersions, but finding a negligible coefficient for the q^3-term, suggesting that lattice anharmonicity can be described by q-dependency. The solid curves in Fig. 4(b) represent the fitting of the data using the equation $E(q) = E_h \sin(q\pi) - E_a q - E_{e-p} q^2$, where q is the wavevector in dimensionless reciprocal lattice units (r.l.u.), E_a is the anharmonic energy at the zone boundary, and E_{e-p} is the scattering energy near the zone boundary. For the LA mode at 610 K, the fitting yields E_h = 16.8(2) meV, E_a = 1.15(6) meV, and E_{e-p} = 6.53(1) meV. For the TA mode, the fitting parameters obtained are E_h = 12.0(4) meV, E_a = 0.93(4) meV, and E_{e-p} = 6.98(1) meV. It is evident that E_{e-p} is ~6 times higher than E_a. Notably, E_a is associated with three-phonon scattering arising from third-order atomic displacements. Higher-order multi-phonon scattering would not be stronger than the three-phonon scattering described by the q-dependency. Hence, another source of scattering must be present in this material system.

Moreover, q^2 dependency is a characteristic of the conduction-electron energy dispersion, and the thermal variations of the observed E_{e-p} for both the LA and TA phonons can be described using a Fermi–Dirac thermal distribution, similar to a degenerate semiconductor where the donor band overlaps with the conduction band. This behavior is observed in the heavily doped

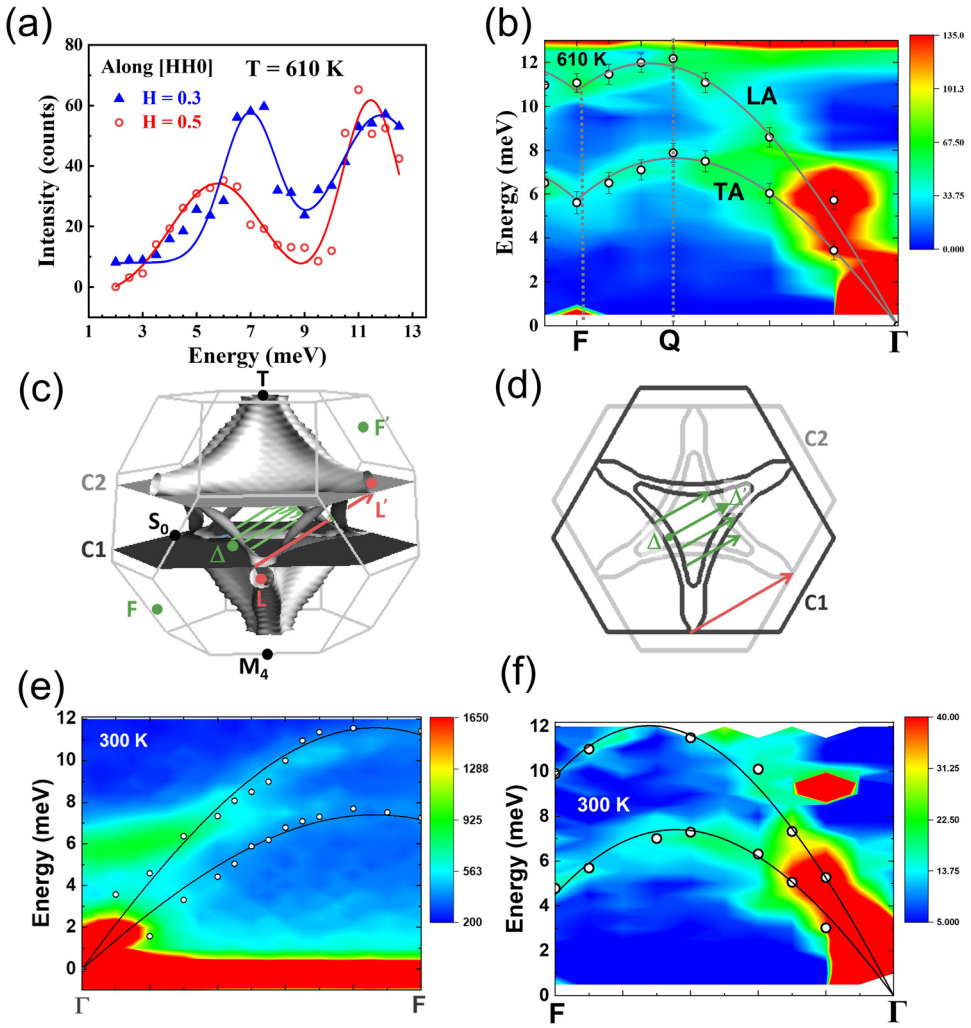

Fig. 4 Phonon dispersion and density of state relations. (a) Phonon excitation spectra measured in constant-Q scans along the crystallographic [HH0] direction at H = 0.3 (filled triangles) and 0.5 (open circles) at 610 K. (b) Phonon dispersion of $(Ge_{0.86}Sb_{0.08}Bi_{0.06})Te$ at 610 K, measured along the crystallographic [110] direction. (c) Calculated Fermi surface of p-type GeTe at the Fermi energy, E_{f0}, slightly lower than Δ maximum, as indicated in Fig. 5(b). (d) The two corresponding 2D cross-sections (C1 and C2) of the Fermi surface. The short green arrows and the long red arrow indicate the wave vector difference $\Delta\boldsymbol{k}$ between the initial and final states due to the electronic transition in the [110] direction (the $\Gamma \rightarrow F$ direction). Images of (c) and (d) are prepared by using FermiSurfer. (e) Phonon dispersion of pristine GeTe at 300 K. (f) Phonon dispersion of Sb–Bi codoped GeTe at 300 K.

$(Ge_{0.86}Sb_{0.08}Bi_{0.06})Te$.[54] Therefore, it is concluded that the $R3m$ phase exhibits a strong EP interaction characterized by E_{e-p}.

The phonon lifetime, denoted as τ, can be determined from INS measurements by using the width of the phonon excitation profile. The relation is given by $\tau = (\pi \cdot W)^{-1}$, where W represents the full-width-at-half-maximum of the intrinsic excitation profile.[55] In the case of $(Ge_{0.86}Sb_{0.08}Bi_{0.06})Te$, the widths of the phonon excitation profiles obtained from INS measurements are significantly broader than the instrumental resolution function. This indicates short phonon lifetimes on the order of 1 ps at 610 K (Fig. S21, ESI†). The short phonon lifetimes are consistent with the representative value of 1.1 ps obtained from the κ_{lat} measurement and phonon dispersion calculated using first-principles methods, as discussed in the ESI† (statistically representative value of the phonon mean free path). Short phonon propagation lengths limit heat transport, which results in low thermal conductivity in the $(Ge_{0.86}Sb_{0.08}Bi_{0.06})Te$ crystal.

Strong Kohn anomaly in Sb–Bi codoped GeTe

As shown in Fig. 4(c) and Fig. S3 (ESI†), when the Fermi level is slightly lower than the Δ maximum (Fig. 5(b) and Fig. S3c, ESI†), the electronic structure shows 1D-like behavior. This means that the energies of electronic states strongly depend on the wavevector ($\mathbf{k}$) along a single axis. In semiconductors, such 1D-like behavior in the electronic structure gives rise to a characteristic feature known as the double-walled Fermi surface. This refers to a pair of Fermi surfaces that are nearly parallel to each other and located in close proximity. When Fermi surfaces are considered nested, it means that there is a significant overlap or matching of electronic states between the two parallel Fermi surfaces. This nesting property has

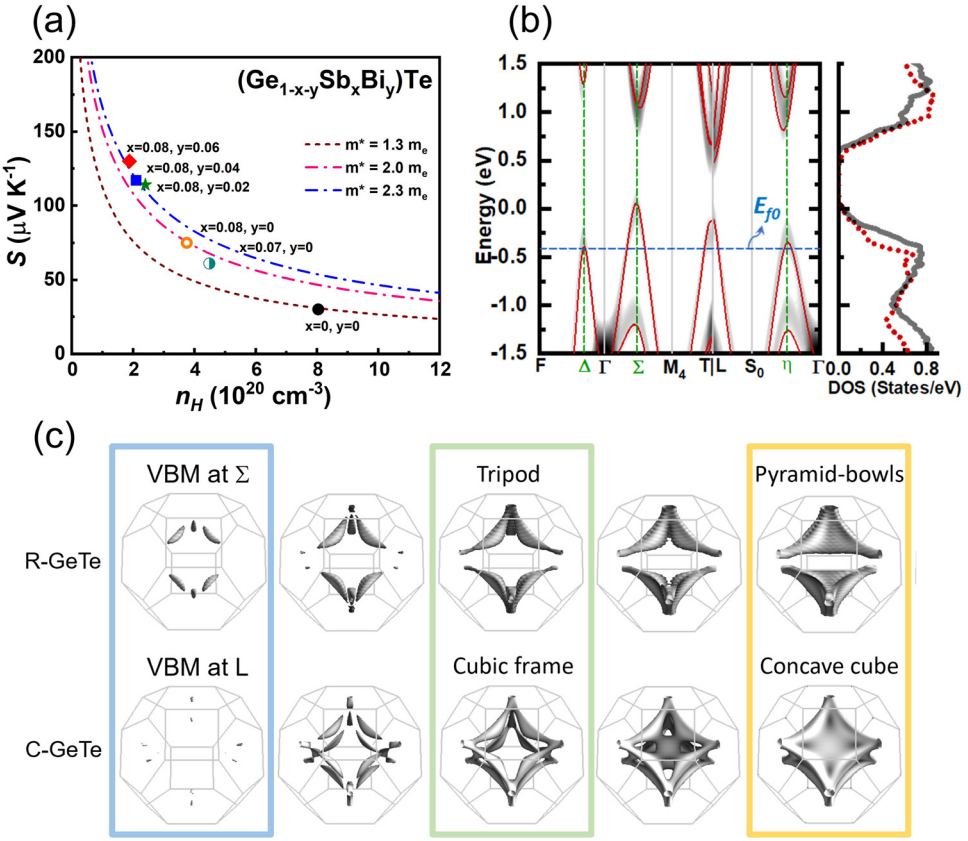

Fig. 5 Electronic structure and Fermi surfaces. (a) Pisarenko plot of $(Ge_{1-x-y}Sb_xBi_y)Te$ at 300 K showing the increase in DOS effective mass m^* with Sb and Bi codoping. (b) Electronic structures of pristine GeTe (red bands) and Sb–Bi codoped ($Ge_{24}Sb_2Bi_1Te_{27}$) unfolded to the GeTe Brillouin zone (gray bands). The corresponding crystal structure can be seen in Fig. S20 (ESI†). Their density of states (DOS) is shown by red and gray lines in the right panel, respectively. (c) Evolution of the Fermi surface of p-type GeTe in rhombohedral and cubic phases (R-GeTe and C-GeTe).

important implications for the electronic and thermal transport properties of the material, as it can give rise to enhanced EP interactions, leading to phenomena such as charge density waves and Kohn anomaly.[37,56]

The formation of Femi surface nesting occurs when the Fermi level is lower than the energy of the Δ pocket. As will be discussed later, the presence of Sb/Bi dopants can increase the energy of the Δ pocket, enabling the formation of Fermi surface nesting. This suggests that Sb–Bi codoped GeTe can exhibit a stronger EP interaction compared to pristine GeTe, despite the latter having a higher hole concentration (Fig. S24a, ESI†). The strong EP interaction is confirmed by the phonon dispersion obtained from the INS measurements on Sb–Bi codoped GeTe (Fig. 4(b) and (e)) and pristine GeTe (Fig. 4(f)). As can be seen, the Sb–Bi codoped sample exhibits a significant Kohn anomaly in the phonon dispersion, whereas the pristine sample does not show such a feature. The Kohn anomaly serves as a characteristic signature of the strong EP interaction. Its presence in the phonon dispersion of the Sb–Bi codoped GeTe suggests that the EP interaction is significantly enhanced in this material. Conversely, the absence of a Kohn anomaly in the pristine GeTe indicates a weaker EP interaction in comparison.

The momentum conservation plays a crucial role in the interaction between phonons and electrons. In the case of Fermi surface nesting, when the wave vector $\boldsymbol{q}$ of the interacting phonons is equal to $\Delta\boldsymbol{k}$, which represents the momentum transfer between the nested Fermi surfaces, a renormalization of phonon energy occurs due to the strong EP interaction.[51] Such anomaly was observed along the Γ–F direction by INS (Fig. 4(b) and (f)). In the process of electron–phonon scattering, the crystal momentum change due to the electronic transition, $\hbar\Delta\boldsymbol{k}$, and due to the phonon creation/annihilation, $\hbar\Delta\boldsymbol{q}$, should satisfy $\Delta\boldsymbol{k} + \Delta\boldsymbol{q} = \boldsymbol{G}$. The smallest $\Delta\boldsymbol{k}$ along the ΓF direction corresponding to the electronic transition between states around Δ and Δ' is about $0.35\boldsymbol{G}_0$. Due to the nesting feature of both the interior and exterior of the bowl-shaped Fermi surface around Δ (Δ'), several nesting vectors can be identified as indicated by the green arrows in Fig. 4(c) and (d). Here, $\boldsymbol{G}_0$ is the reciprocal lattice vector in the [110] direction. $\Delta\boldsymbol{k}$ can stretch to $0.5\boldsymbol{G}_0$, which is the F point, when the initial/final states deviate from Δ/Δ' to L/L' as indicated by the red arrow in Fig. 4(c) and (d). The Fermi surface nesting vectors thus begin near the phonon wavevector, $0.35\boldsymbol{G}_0$, of Q in Fig. 4(b) and continue to that, $0.35\boldsymbol{G}_0$, of F. Similar results are also found in C-GeTe as shown in Fig. S3b (ESI†). The quantitative agreement between the measured softened phonon wave vectors and the electronic nesting vectors confirms that the EP interaction is the cause leading to the observed energy reduction in the

phonon modes. It is noted that the above discussion considers the EP scattering processes only when involving the creation/annihilation of a single phonon. Those involving two phonons, as discussed in the ESI† (electron–phonon scattering processes causing a downturn in phonon dispersion), would further strengthen the Kohn anomaly around the F point due to the enormous number of channels of the intra-bowl electronic transitions, and all these scattering processes lead to the reduction in the lattice thermal conductivity improving the thermoelectric performance.

Similar results are also observed in C-GeTe, as depicted in Fig. S3 (ESI†). The agreement between the measured softened phonon wave vectors and the electronic nesting vectors provides quantitative evidence supporting the EP interaction as the underlying mechanism responsible for the energy reduction in the phonon modes. It is important to note that the previous discussion focused on EP scattering processes involving the creation or annihilation of a single phonon. However, the ESI† (EP scattering processes causing a downturn in the phonon dispersion) highlights the significance of two-phonon scattering processes in further enhancing the Kohn anomaly around the F point. Due to the large number of channels available for intra-bowl electronic transitions, these two-phonon processes contribute significantly to the strengthening of the Kohn anomaly. The combined effect of both single and two-phonon scattering processes leads to a reduction in lattice thermal conductivity, which, in turn, improves the thermoelectric performance of the material.

Enhanced Seebeck coefficient and low-dimensional behavior

The Pisarenko relation at 300 K, as shown in Fig. 5(a) demonstrates that Sb–Bi codoping GeTe exhibits an effective mass of 2.3 m_e much larger than 1.3 m_e of the pristine GeTe. This result indicates that the enhancement of the Seebeck coefficient in Sb–Bi codoped GeTe is not solely due to the shifting of the Fermi level (E_f), but also due to a band convergence resulting from Sb–Bi codoping. Fig. 5(b) presents the electronic structure of both undoped and Sb–Bi codoped GeTe. It is evident that the introduction of Sb and Bi dopants in R-GeTe leads to an increase in the valence band maximum (VBM) energy at the Δ maximum, resulting in the simultaneous convergence of $L(T)$, Σ, and Δ bands. This band convergence is experimentally confirmed by an increase in the density of states of effective mass (m^*) shown in Fig. 5(a), as well as the computed DOS depicted in Fig. 5(b).

Considering that the electronic structure below the Δ maximum exhibits a 1D-like behavior, the increase in the energy of the Δ maximum leads to a significant enhancement in the DOS for Sb–Bi codoped GeTe compared to pristine GeTe as the energy decreases. It is known that certain cubic IV–VI semiconductors, including cubic GeTe (C-GeTe), exhibit a primary valence band at the L point in the Brillouin zone, along with a secondary valence band along the Σ line (Fig. 5(c)). As the Fermi level moves deeper into the valence bands, Fermi surface pockets at Σ, in addition to those at L, merge to form tube-like Fermi surfaces within the cubic frame (indicated by the green box in Fig. 5(c)). These tube-like Fermi surfaces arise from a 2D-like electronic structure, where the electronic states exhibit strong **k**-dependence along only two axes. This leads to a highly effective valley degeneracy, which has been observed to contribute to record-breaking thermoelectric performance in materials such as PbTe, PbSe, and SnTe.[57] The tube-like Fermi surfaces with high effective valley degeneracy provide favorable conditions for enhancing thermoelectric properties. They enable efficient energy and charge transport through the material, leading to an improved Seebeck coefficient. Additionally, the high valley degeneracy allows for more opportunities for electron and phonon scattering, which can lead to reduced lattice thermal conductivity and enhanced thermoelectric efficiency.

In Fig. 5(c), the evolution of the Fermi surface with a decrease in the Fermi level for p-type GeTe in the rhombohedral structure is depicted, highlighting its similarity to the low-dimensional behavior observed in cubic GeTe (C-GeTe). The rhombohedral distortion in GeTe (R-GeTe) causes the Σ band to be located at higher energy, resulting in the formation of the first Fermi surface consisting of six elliptical pockets with strong anisotropy (indicated by the blue box in Fig. 5(c)). As the cubic structural transitions to the rhombohedral structure, the rhombohedral distortion breaks the degeneracy of the 12 Σ pockets observed in C-GeTe, reducing them to six Σ pockets. Additionally, there are six similar pockets located at lower energy along the η line (Γ–S_0) in R-GeTe (Fig. 5(b)). These elliptical Fermi surfaces at Σ eventually reach the Brillouin zone edge and merge with the valence band pockets at the distorted L and T points, which are equivalent in C-GeTe, thereby resulting in the formation of two tripods with a total of six tube-like (2D-like) legs within the Brillouin zone (indicated by the green box in Fig. 5(c)).

In C-GeTe, the Fermi surface exhibits similar characteristics. The first valence band maximum (VBM) is located at the L points (as shown in Fig. S12b, ESI†), which then merges with the Σ band, forming a cubic frame with 12 tube-like (2D-like) edges as more holes are added. Because the $\Sigma(L)$ pocket is in higher energy than the $L(\Sigma)$ pocket in R-GeTe (C-GeTe) (Fig. S12, ESI†), the L–Σ band convergence can be achieved by introducing Sb/Bi dopants, which causes the crystal structure to be more cubic-like (as shown in Fig. S6b, ESI†). As the Fermi level decreases to E_{f0}, an energy slightly lower than the maximum of the Δ band in R-GeTe, the tube-like legs of the tripod expand laterally and connect with each other. This leads to the evolution of the Fermi surface from the tube-like (2D-like) legs of the tripod into a double-walled (3D-like) pyramid-bowl shape as depicted by the blue and yellow boxes in Fig. 5(c). The edges and corners of the Fermi surface around Σ and L correspond to the successors of the legs and vertices of the tripod structure.

The formation of the double-walled pyramid bowls indicates a shift in the geometric topology from a 2D-like electronic structure to a 1D-like electronic structure, where the **k** dependence is primarily along only one axis. This transition results in a dramatic increase in the DOS below the energy of the Δ maximum, resembling the behavior of a 1D system (as shown

in Fig. 5(b), 1(a) and Fig. S3, ESI†). The presence of a 1D-like electronic structure in these materials plays a crucial role in achieving high valley degeneracy and Fermi surface nesting, which in turn leads to exceptional thermoelectric performance characterized by a large power factor and low thermal conductivity. To understand the fundamental origin of this unique 1D-like electronic structure, it is necessary to examine the wave functions in the vicinity of the Δ point. The ESI† on wave functions of 1D-like electronic states provides a detailed analysis of the wave functions of the electronic states at the Δ point. It is observed that these wave functions exhibit a parallel chain-like shape with limited inter-chain overlap, resembling dense nanowires. This limited inter-chain overlap is responsible for the manifestation of the 1D-like feature in the electronic structure.

Conclusions

In this study, we report the first Sb–Bi codoped GeTe crystal $(Ge_{0.86}Sb_{0.08}Bi_{0.06})Te$ with an ultrahigh $zT \approx 2.7$ at 700 K and a record high device zT of 1.41 in the temperature range of 300–773 K. Our INS measurements discovered a Kohn anomaly indicating strong EP interactions in the material. DFT analysis demonstrates the Fermi nesting in the low dimensional Fermi surface with high valley degeneracy as the origin of the strong EP interactions leading to the observed extremely low lattice thermal conductivity and high zT. A better band convergence as well as more well-tuned hole concentration would be achieved by further introducing other dopants such as Mg, Ag, Cu, and In, and a further improvement of zT can be realized. Based on our analysis, an ultrahigh zT is expected not only in GeTe-based alloys but other IV–VI materials such as PbTe, SnTe, and SnSe with similar electronic behaviors. The implications of this research transcends the current findings based on but not limited to single crystals, providing a groundbreaking roadmap for achieving unparalleled thermoelectric performance in materials. Through the revelation of the intricacies of the EP interaction and its interconnectedness with a Fermi surface topology, our study charts a course for deliberate advancements in the design of thermoelectric materials. This newfound understanding is poised to inspire continued exploration and innovation, propelling the field toward heightened energy conversion technologies and sustainable solutions.

Experimental procedures

Sample synthesis

The precursors of the Ge ingot (99.999%), Sb shot (99.999%), Te shot (99.999%), and Bi shot (99.999%) from Alfa Aesar were purified before synthesis. In the series of $(Ge_{1-x-y}Sb_xBi_y)Te$ crystals, we fixed the Sb composition at $x = 0.08$ according to our previously reported results.[39] $(Ge_{1-x-y}Sb_xBi_y)Te$ with $x = 0$ and 0.08 and $y = 0$, 0.02, 0.04, and 0.06 were synthesized by a two-step process. In the first step, pure elements were sealed in a 13 mm diameter quartz tube under a high vacuum of $\sim 3 \times 10^{-6}$ torr. The samples were heated at 1223 K for 48 h to homogenize the molten liquid, and then the furnace cooled to room temperature. The obtained $(Ge_{1-x-y}Sb_xBi_y)Te$ ingots were ground into small pieces and sealed in conical shaped quartz tubes under a high vacuum. To avoid the thermal expansion breakage of samples, the sealed tubes were loaded into another bigger round-shaped tube and loaded in a Bridgman furnace at 1123 K. The growth rate of crystals is set as 3 mm h^{-1}. The obtained crystals were approximately 50–60 mm in length and 10 mm in diameter. The size allows all thermoelectric property measurements in the same direction.

Structure characterization and thermoelectric property measurements

The structural phase of crystals was examined by X-ray diffraction, performed with a diffractometer (XRD, PANalytical X'Pert Pro) equipped with Cu Kα radiation (λ = 1.5406 Å). The lattice parameters were calculated using Rietveld refinement from the Highscore Plus program. The crystal orientation of samples was analyzed using a triple-axis X-ray diffractometer (Malvern Panalytical's Materials Research Diffractometers, MRD) and a Laue diffractometer (IPX-YGR-LC). The surface morphology and chemical compositions of the crystals were investigated using an SEM (Inspect F FEI) equipped with an energy-dispersive X-ray (EDX) spectrometer. For TEM observation, the crystal sample with 50–80 nm thickness was cut from bulk ingots using a focused ion beam instrument (Hitachi NX2000). The TEM micrographs and SAED patterns were acquired using a spherical aberration-corrected transmission electron microscope (JEOL-ARM 200FTH) operating at 200 kV. The Seebeck coefficient and electrical conductivity were measured using a static dc method using a commercial instrument (ZEM-3, ULVAC-RIKO). The uncertainty for the electrical conductivity is 3%, and the Seebeck coefficient is 5%. Thermal conductivity was calculated by $\kappa = D\rho C_p$, where D is the thermal diffusivity, ρ is the mass density measured by the Archimedes method, and C_p is the specific heat measured using a differential scanning calorimeter (DSC, Q100, TA Instruments). The thermal diffusivity was measured by the laser flash method (LFA-457, NETZSCH). The uncertainty of the thermal conductivity is 5%. Combining several uncertainties from electrical conductivity, Seebeck coefficient, and thermal conductivity, the total uncertainty of zT is about 18%. The room temperature Hall carrier concentration is calculated from the Hall coefficient obtained by sweeping the magnetic field from -5 T to +5 T using a Physical Property Measurement System (PPMS, Quantum Design). The uncertainty of the Hall coefficient is $\sim$3%.

Inelastic neutron scattering measurements

Single crystal inelastic neutron scattering measurements were conducted at ANSTO, employing the cold neutron triple-axis spectrometer SIKA with the energy of neutrons defined by PG (002) crystals at both the monochromator and analyzer positions, a fixed final energy of 8.07 meV, and a Be filter to suppress higher-order contaminations. The crystal was aligned for the a–b scattering plane, and the temperature was

controlled using a CF-7 cryofurnace system with a slow heating rate of 10 K min^{-1}. Neutron wavevector transfer was denoted as $\mathbf{Q}(Q_hQ_kQ_l) = \mathbf{G}(hkl) + \mathbf{q}(HKL)$, where $\mathbf{G}$ is a reciprocal lattice vector and $\mathbf{q}$ is the phonon wavevector.

Theoretical calculation

Detailed methods of theoretical calculations are provided in the ESI,† encompassing sections on electronic structures, electronic transport properties, lattice thermal conductivity, phonon dispersion, and electron–phonon coupling.

Author contributions

V. K. R. and C. L. C. prepared the single-crystal samples, and carried out the TEM characterization and thermoelectric-property measurements. T. H. W., A. H., and H. T. J. performed the theoretical calculations. M. H. M., C. M. W. and W. H. L. performed the neutron scattering measurements and data analysis. W. H. T., T. L. H., M. N. O., C. H. L., and K. H. C. provided the technical support for experiments. M. K. B. and G. J. S. provided useful inputs on the understanding of low-dimensional electronic structures. Y. Y. C. conceived the project and led the whole team, and co-edited the manuscript with the assistance of C. L. C., T. H. W., and H. T. J. to successfully accomplish the project. All authors contributed to the manuscript preparation and writing.

Conflicts of interest

All authors declare no competing interests.

Acknowledgements

We acknowledge helpful discussions with Prof. Mei-Yin Chou on the interpretation of neutron data. This work was financially supported by Ministry of Science and Technology (MOST), Taiwan, Grant No. MOST 110-2112-M-001-080, MOST 109-2112-M-001-047, MOST 109-2112-M-007-034-MY3, MOST 111-2112-M-001-080, NSTC 112-2112-M-131-002-MY3, NSTC 109-2112-M-005-014-MY3, NSTC 112-2112-M-007-034-MY3, NSTC 112-2112-M-001-076, and the research grant from Academia Sinica and iSNR-NCHU-MOE, AS-SS-109-01-110. H.T.J. also thanks support from NCHC, CINCNTU, AS-iMATE-111-12, and CQT-NTHU-MOE, Taiwan.

References

1 G. J. Snyder, S. LeBlanc, D. Crane, H. Pangborn, C. E. Forest, A. Rattner, L. Borgsmiller and S. Priya, Distributed and localized cooling with thermoelectrics, *Joule*, 2021, **5**, 748–751.
2 L. E. Bell, Cooling, heating, generating power, and recovering waste heat with thermoelectric systems, *Science*, 2008, **321**, 1457–1461.
3 G. J. Snyder and E. S. Toberer, Complex thermoelectric materials, *Nat. Mater.*, 2008, **7**, 105–114.
4 S. I. Kim, K. H. Lee, H. A. Mun, H. S. Kim, S. W. Hwang, J. W. Roh, D. J. Yang, W. H. Shin, X. S. Li, Y. H. Lee, G. J. Snyder and S. W. Kim, Dense dislocation arrays embedded in grain boundaries for high-performance bulk thermoelectrics, *Science*, 2015, **348**, 109–114.
5 M. N. Hasan, H. Wahid, N. Nayan and M. S. M. Ali, Inorganic thermoelectric materials: A review, *Int. J. Energy Res.*, 2020, **44**, 6170–6222.
6 M. Hong, Z. G. Chen, L. Yang, Z. M. Liao, Y. C. Zou, Y. H. Chen, S. Matsumura and J. Zou, Achieving $zT > 2$ in p-type $AgSbTe_{2-x}Se_x$ alloys via exploring the extra lght valence band and introducing dense stacking faults, *Adv. Energy Mater.*, 2017, **8**, 1702333.
7 K. Biswas, J. He, I. D. Blum, C. I. Wu, T. P. Hogan, D. N. Seidman, V. P. Dravid and M. G. Kanatzidis, High-performance bulk thermoelectrics with all-scale hierarchical architectures, *Nature*, 2012, **489**, 414–418.
8 H. Liu, X. Yuan, P. Lu, X. Shi, F. Xu, Y. He, Y. Tang, S. Bai, W. Zhang, L. Chen, Y. Lin, L. Shi, H. Lin, X. Gao, X. Zhang, H. Chi and C. Uher, Ultrahigh thermoelectric performance by electron and phonon critical scattering in $Cu_2Se_{1-x}I_x$, *Adv. Mater.*, 2013, **25**, 6607–6612.
9 C. Chang, M. Wu, D. He, Y. Pei, C. F. Wu, X. Wu, H. Yu, F. Zhu, K. Wang, Y. Chen, L. Huang, J. F. Li, J. He and L. D. Zhao, 3D charge and 2D phonon transports leading to high out-of-plane zT in n-type SnSe crystals, *Science*, 2018, **360**, 778–783.
10 Z. Bu, X. Zhang, B. Shan, J. Tang, H. Liu, Z. Chen, S. Lin, W. Li and Y. Pe, Realizing a 14% single-leg thermoelectric efficiency in GeTe alloys, *Sci. Adv.*, 2021, **7**, eabf2738.
11 M. Hong, K. Zheng, W. Lyv, M. Li, X. Qu, Q. Sun, S. Xu, J. Zou and Z. G. Chen, Computer-aided design of high-efficiency GeTe-based thermoelectric devices, *Energy Environ. Sci.*, 2020, **13**, 1856–1864.
12 S. Roychowdhury, T. Ghosh, R. Arora, M. Samanta, L. Xie, N. K. Singh, A. Soni, J. He, U. V. Waghmare and K. Biswas, Enhanced atomic ordering leads to high thermoelectric performance in $AgSbTe_2$, *Science*, 2021, **371**, 722–727.
13 C. Liu, Z. Zhang, Y. Peng, F. Li, L. Miao, E. Nishibori, R. Chetty, X. Bai, R. Si, J. Gao, X. Wang, Y. Zhu, N. Wang, H. Wei and T. Mori, Charge transfer engineering to achieve extraordinary power generation in GeTe-based thermoelectric materials, *Sci. Adv.*, 2023, **9**, eadh0713.
14 C. Cho, B. Kim, S. Park and E. Kim, Bisulfate transport in hydrogels for self-healable and transparent thermoelectric harvesting film, *Energy Environ. Sci.*, 2022, **15**, 2049–2060.
15 D. H. Kim, Z. A. Akbar, Y. T. Malik, J. W. Jeon and S. Y. Jang, Self-healable polymer complex with a giant ionic thermoelectric effect, *Nat. Commun.*, 2023, **14**, 3246.
16 C. G. Han, X. Qian, Q. Li, B. Deng, Y. Zhu, Z. Han, W. Zhang, W. Wang, S. P. Feng, G. Chen and W. Liu, Giant thermopower of ionic gelatin near room temperature, *Science*, 2020, **368**, 1091–1098.

17 E. D. Eastman, Theory of the soret effect, *J. Am. Chem. Soc.*, 1928, **50**, 283–291.
18 R. Zito Jr., Thermogalvanic energy conversion, *AIAA J.*, 1963, **1**, 2133–2138.
19 Y. Tian, X. Yang, K. Li, Q. Zhang, Y. Li, H. Wang and C. Hou, High-performance ionic thermoelectric materials and emerging applications of ionic thermoelectric devices, *Mater. Today. Energy*, 2023, **36**, 101342.
20 G. J. Snyder, A. H. Snyder, M. Wood, R. Gurunathan, B. H. Snyder and C. Niu, Weighted mobility, *Adv. Mater.*, 2020, **32**, e2001537.
21 A. Zevalkink, D. M. Smiadak, J. L. Blackburn, A. J. Ferguson, M. L. Chabinyc, O. Delaire, J. Wang, K. Kovnir, J. Martin, L. T. Schelhas, T. D. Sparks, S. D. Kang, M. T. Dylla, G. J. Snyder, B. R. Ortiz and E. S. Toberer, A practical field guide to thermoelectrics: Fundamentals, synthesis, and characterization, *Appl. Phys. Rev.*, 2018, **5**, 021303.
22 L. D. Hicks, T. C. Harman, X. Sun and M. S. Dresselhaus, Experimental study of the effect of quantum-well structures on the thermoelectric figure of merit, *Phys. Rev. B: Condens. Matter Mater. Phys.*, 1996, **53**, 10493–10496.
23 L. D. Hicks and M. S. Dresselhaus, Thermoelectric figure of merit of a one-dimensional conductor, *Phys. Rev. B: Condens. Matter Mater. Phys.*, 1993, **47**, 16631–16634.
24 A. Li, C. Hu, B. He, M. Yao, C. Fu, Y. Wang, X. Zhao, C. Felser and T. Zhu, Demonstration of valley anisotropy utilized to enhance the thermoelectric power factor, *Nat. Commun.*, 2021, **12**, 5408.
25 M. S. Dresselhaus, G. Chen, M. Y. Tang, R. Yang, H. Lee, D. Wang, Z. Ren, J. P. Fleurial and P. Gogna, New directions for low-dimensional thermoelectric materials, *Adv. Mater.*, 2007, **19**, 1043–1053.
26 J. P. Heremans, C. M. Thrush, D. T. Morelli and M. C. Wu, Thermoelectric power of bismuth nanocomposites, *Phys. Rev. Lett.*, 2002, **88**, 216801.
27 J. E. Cornett and O. Rabin, Thermoelectric figure of merit calculations for semiconducting nanowires, *Appl. Phys. Lett.*, 2011, **98**, 182104.
28 C. J. Vineis, A. Shakouri, A. Majumdar and M. G. Kanatzid, Nanostructured thermoelectrics: big efficiency gains from small features, *Adv. Mater.*, 2010, **22**, 3970–3980.
29 M. T. Dylla, S. D. Kang and G. J. Snyder, Effect of two-dimensional crystal orbitals on Fermi surfaces and electron transport in three-dimensional perovskite oxides, *Angew. Chem., Int. Ed.*, 2018, **58**, 5503–5512.
30 D. Parker, X. Chen and D. J. Singh, High three-dimensional thermoelectric performance from low-dimensional bands, *Phys. Rev. Lett.*, 2013, **110**, 146601.
31 M. K. Brod and G. J. Snyder, Orbital chemistry of high valence band convergence and low-dimensional topology in PbTe, *J. Mater. Chem. A*, 2021, **9**, 12119–12139.
32 B. Liao, B. Qiu, J. Zhou, S. Huberman, K. Esfarjani and G. Chen, Significant reduction of lattice thermal conductivity by the electron-phonon interaction in silicon with high carrier concentrations: a first-principles study, *Phys. Rev. Lett.*, 2015, **114**, 115901.
33 J. Zhou, H. D. Shin, K. Chen, B. Song, R. A. Duncan, Q. Xu, A. A. Maznev, K. A. Nelson and G. Chen, Direct observation of large electron–phonon interaction effect on phonon heat transport, *Nat. Commun.*, 2020, **11**, 6040.
34 C. Li, N. K. Ravichandran, L. Lindsay and D. Broido, Fermi surface nesting and phonon frequency gap drive anomalous thermal transport, *Phys. Rev. Lett.*, 2018, **121**, 175901.
35 H. Liu, C. Yang, B. Wei, L. Jin, A. Alatas, A. Said, S. Tongay, F. Yang, A. Javey, J. Hong and J. Wu, Anomalously suppressed thermal conduction by electron-phonon coupling in charge-density-wave tantalum disulfide, *Adv. Sci.*, 2020, **7**, 1902071.
36 L. Hu, Y. W. Fang, F. Qin, X. Cao, X. Zhao, Y. Luo, D. V. M. Repaka, W. Luo, A. Suwardi, T. Soldi, U. Aydemir, Y. Huang, Z. Liu, K. Hippalgaonkar, G. J. Snyder, J. Xu and Q. Yan, High thermoelectric performance enabled by convergence of nested conduction bands in $Pb_7Bi_4Se_{13}$ with low thermal conductivity, *Nat. Commun.*, 2021, **12**, 4793.
37 W. Kohn, Image of the Fermi surface in the vibration spectrum of a metal, *Phys. Rev. Lett.*, 1959, **2**, 393–394.
38 B. Jiang, W. Wang, S. Liu, Y. Wang, C. Wang, Y. Chen, L. Xie, M. Huang and J. He, High figure-of-merit and power generation in high-entropy GeTe-based thermoelectrics, *Science*, 2022, **377**, 208–213.
39 R. K. Vankayala, T. W. Lan, P. Parajuli, F. Liu, R. Rao, S. H. Yu, T. L. Hung, C. H. Lee, S. Yano, C. R. Hsing, D. L. Nguyen, C. L. Chen, S. Bhattacharya, K. H. Chen, M. N. Ou, O. Rancu, A. M. Rao and Y. Y. Chen, High zT and Its origin in Sb-doped GeTe single crystals, *Adv. Sci.*, 2020, **7**, 2002494.
40 G. J. Snyder and A. H. Snyder, Figure of merit zT of a thermoelectric device defined from materials properties, *Energy Environ. Sci.*, 2017, **10**, 2280–2283.
41 L. D. Zhao, S. H. Lo, Y. Zhang, H. Sun, G. Tan, C. Uher, C. Wolverton, V. P. Dravid and M. G. Kanatzidis, Ultralow thermal conductivity and high thermoelectric figure of merit in SnSe crystals, *Nature*, 2014, **508**, 373–377.
42 S. I. Kim, K. H. Lee, H. A. Mun, H. S. Kim, S. W. Hwang, J. W. Roh, D. J. Yang, W. H. Shin, X. S. Li, Y. H. Lee, G. J. Snyder and S. W. Kim, Dense dislocation arrays embedded in grain boundaries for high-performance bulk thermoelectrics, *Science*, 2015, **348**, 109–114.
43 S. Roychowdhury, R. Panigrahi, S. Perumal and K. Biswas, Ultrahigh thermoelectric figure of merit and enhanced mechanical stability of p-type $AgSb_{1-x}Zn_xTe$, *ACS Energy Lett.*, 2017, **2**, 349–356.
44 M. Samanta and K. Biswas, Low thermal conductivity and high thermoelectric performance in $(GeTe)_{1-2x}(GeSe)_x$-$(GeS)_x$: competition between solid solution and phase separation, *J. Am. Chem. Soc.*, 2017, **139**, 9382–9391.
45 D. Kraemer, J. Sui, K. McEnaney, H. Zhao, Q. Jie, Z. F. Ren and G. Chen, *Energy Environ. Sci.*, 2015, **8**, 1299–1308.
46 H. J. Wu, L. D. Zhao, F. S. Zheng, D. Wu, Y. L. Pei, X. Tong, M. G. Kanatzidis, J. Q. He and H. J. Wu, Broad temperature plateau for thermoelectric figure of merit $zT > 2$ in phase-separated PbTe0.7S0.3, *Nat. Commun.*, 2014, **5**, 4515.

47 S. Wang, J. Yang, L. Wu, P. Wei, J. Yang, W. Zhang and Y. Grin, *Chem. Mater.*, 2015, **27**, 1071–1081.
48 K. Biswas, J. He, I. D. Blum, C. I. Wu, T. P. Hogan, D. N. Seidman, V. P. Dravid and M. G. Kanatzidis, High-performance bulk thermoelectrics with all-scale hierarchical architectures, *Nature*, 2012, **489**, 414–418.
49 G. J. Snyder, M. Christensen, E. Nishibori, T. Caillat and B. B. Iversen, Disordered zinc in Zn_4Sb_3 with phonon-glass and electron-crystal thermoelectric properties, *Nat. Mater.*, 2004, **3**, 458–463.
50 P. C. Wei, C. X. Cai, C. R. Hsing, C. M. Wei, S. H. Yu, H. J. Wu, C. L. Chen, D. H. Wei, D. L. Nguyen, M. M. C. Chou and Y. Y. Chen, Enhancing thermoelectric performance by Fermi level tuning and thermal conductivity degradation in $(Ge_{1-x}Bi_x)Te$ crystals, *Sci. Rep.*, 2019, **9**, 8616.
51 D. G. Cahill, S. K. Watson and R. O. Pohl, Lower limit to the thermal conductivity of disordered crystals, *Phys. Rev. B: Condens. Matter Mater. Phys.*, 1992, **46**, 6131–6140.
52 M. Liu, J. Zhu, B. Cui, F. Guo, Z. Liu, Y. Zhu, M. Guo, Y. Sun, Q. Zhang, Y. Zhang, W. Cai and J. Sui, High-performance lead-free cubic GeTe-based thermoelectric alloy, *Cell Rep. Phys. Sci.*, 2022, **3**, 100902.
53 J. Callaway, Model for Lattice thermal conductivity at low temperatures, *Phys. Rev.*, 1959, **113**, 1046–1051.
54 M. H. Ma, C. M. Wu, T. Y. Ling, E. Batsaikhan, W. H. Li, V. K. Ranganayakulu and Y. Y. Chen, Extremely space- and time-limited phonon propagation from electron-lattice scattering induced by Sb/Bi codoping in $Ge_{0.86}Sb_{0.08}Bi_{0.06}Te$ single crystal, *Phys. Rev. Mater.*, 2021, **5**, 114602.
55 G. Nilsson and G. Nelin, Phonon dispersion relations in Ge at 80° K, *Phys. Rev. B: Solid State*, 1971, **3**, 364–369.
56 F. J. Di Salvo and T. M. Rice, Charge-density waves in transition-metal compounds, *Phys. Today*, 1979, **32**, 32–38.
57 J. Xin, Y. Tang, Y. Liu, X. Zhao, H. Pan and T. Zhu, Valleytronics in thermoelectric materials, *npj Quantum Mater.*, 2018, **3**, 9.